

Computer Design of Quantum Experiments

Hans C. Gundlach

Abstract

Physics and computation form a unique positive feedback loop in the sciences. Developments in physics have provided the silicon transistor and quantum computation. Growth in computation has given physicists the ability to model the world at a much wider range of scales. In this essay, we will look at another dimension of this relationship. We will try to approach computers less as calculators, but as telescopes helping us see conceptually further from the intuitive everyday world we inhabit to the realm of quantum physics. We will investigate this potential by examining the automated design of quantum experiments. The first part of this essay will cover the background needed to understand quantum experiments, including the basics of linear optics and entanglement by path identity. Then we will investigate the connection between graphs and quantum experiments. Using this background, we will explain and compare two automated systems MELVIN and Theseus which offer promising directions in the field of quantum experiment design. Finally, we will look at the bounds of these systems for certain quantum states. In relation to these bounds, the author has developed several novel proofs and simplifications. These new results, which rely on only simple combinatorial principles, are presented in the appendix for the interested reader.

1 Introduction

In this essay we will focus on quantum optical systems this is for two reasons. First, quantum optical techniques offer a promising direction in quantum computing technology. Photonic systems are mobile and low-noise [23]. Recent advances have also made photonic information processing much easier. We will see how non-trivial quantum experiments can be done on a chip a few millimeters in size [6]. Maybe someday we could hold quantum computers in the palm of our hands. The experiments we will explore offer a step in this direction.

Second, quantum optical systems have been an excellent lens into the counter-intuitive aspects of reality. Much of the research into the foundations of quantum mechanics has been tested by looking at the non-intuitive quantum properties of photons including the Bell test of local realism, and the quantum eraser experiment. Quantum optical experiments like boson sampling have also offered some of the starkest demonstrations of quantum supremacy over classical systems. We will look at “crystal networks” which offer a promising alternative to boson sampling in the demonstrations of quantum supremacy [8]. In addition, we will examine systems that are able to design GHZ states. These states are used to demonstrate contradictions with local hidden variable theories of quantum mechanics [4].

The field of quantum experiments especially necessitates automatic design systems. This is due to the fact that the number of possible configuration of quantum experiments combinatorially explodes with larger systems. However, the blind creation and modeling of quantum systems not only poses interpretability issues but is missing one of the central epistemic aims of science: to gain understanding [13]. The final section of this essay will use the concepts developed in the previous sections to examine the power of these automated systems and how to bridge the gap between human and machine insight.

2 Quantum Optics Background

In order to understand photonic experiments we must first understand photons. A photon can have either horizontal (H) or vertical (V) polarization or a superposition of these states. Photons can also be described using right or left circular polarization but we will not be concerned with this representation here. Since polarization comes in only two types (H,V) it is a rather limited basis for photonic quantum experiments.

In order to represent a much wider variety of states, we will also include what is called the orbital angular momentum (OAM). Every beam of light has a given linear momentum P and, therefore, has an angular momentum analogous to the traditional angular momentum $L = r \times P$. OAM modes can represent any integer, and hence we can form the multidimensional analog of qubits “qudits” using this property.

Quantum optical experiments often use a bewildering array of elements. However, in this section I will focus on the beam splitter which plays a crucial role in many optical experiments and is an important tool in state generation. Further, the formalism needed to describe the quantum beam splitter will be useful throughout this article.

A classical beam splitter takes incident light and splits it into transmitted and reflected beams. The quantum mechanical 2-photon beam splitter takes two photons a and b and converts them to two photons c and d. Photons in each input mode can be represented using the Fock-Space formalism as $|1, 1\rangle_{ab} = \hat{a}^\dagger \hat{b}^\dagger |0, 0\rangle_{ab}$. The beam splitter mixes the modes a and b into the output modes c and d. We can represent this process by converting the operators a and b into a mix of the operators c and d using a transformation:

$$\begin{pmatrix} \hat{a} \\ \hat{b} \end{pmatrix} \rightarrow \frac{1}{\sqrt{2}} \begin{pmatrix} 1 & 1 \\ 1 & -1 \end{pmatrix} \begin{pmatrix} \hat{c} \\ \hat{d} \end{pmatrix}. \quad (1)$$

Notice, the -1 component of the matrix. This is a result of the unitarity requirement (observe that this is also a Hadamard transformation). Applying this transformation to the original $|1, 1\rangle_{ab} = \hat{a}^\dagger \hat{b}^\dagger |0, 0\rangle_{ab}$ configuration yields

$$\frac{|2, 0\rangle_{cd} - |0, 2\rangle_{cd}}{\sqrt{2}}. \quad (2)$$

This result is known as the Hong-Ou-Mandel effect and is one of the most important effects in linear optical quantum computing. Unlike a classical beam splitter where inputting two beams of light results in beams of light in both directions, the quantum beam splitter outputs is either in path c or d but not both paths due to destructive interference (transforming the operators a^\dagger and b^\dagger using the matrix above will result in cancellation of terms like $|1, 1\rangle_{cd}$) [2]. This destructive interference is an excellent indicator that quantum effects are at play. Further, the resulting state is an example of a NOON state and is one of the most basic many body entangled states (and has a clear resemblance to the states we will introduce later Sec. 4).

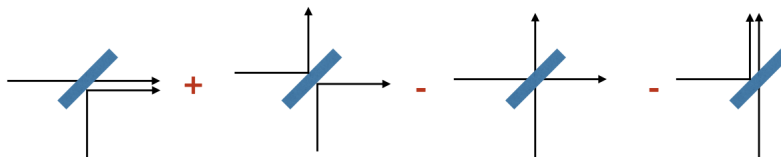


Figure 1: Depiction of the Hong-Ou-Mandel effect. Notice the two middle terms involving photons in both output paths destructively interfere. Image taken from [2].

2.1 Spontaneous Parametric Down Conversion

In order to generate the photons necessary for the experiments explored in this essay, we use a process known as spontaneous parametric down conver-

sion (SPDC). SPDC is a nonlinear optical phenomena whereby a photon of a higher energy referred to as a pump photon collides with crystal and forms two output photon referred to as a signal and idler photon.

The unitary operator that describes the creation of photons in a single crystal is derived from a Hamiltonian (H_{SPDC}) consisting of photon creation operators for paths a and b, a^\dagger and b^\dagger respectively, as well as the down conversion amplitude g (related to the pump power and down conversion rate) [6] i.e

$$H_{SPDC} = g \left(\hat{a}_a^\dagger \hat{a}_b^\dagger \right). \quad (3)$$

Taylor expanding the unitary evolution of the H_{SPDC} Hamiltonian to second order yields an approximation:

$$\begin{aligned} \hat{U}_{a,b} = e^{-i(H_{SPDC}/\hbar)} \approx & 1 + g \left(\hat{a}_a^\dagger \hat{a}_b^\dagger \right) \\ & + \frac{g^2}{2} \left(\hat{a}_a^\dagger \hat{a}_b^\dagger \right)^2 + \mathcal{O}(g^3). \end{aligned} \quad (4)$$

Applying this unitary operator to the vacuum state yields

$$|\psi\rangle = U|vac\rangle = g |a, b\rangle + g^2 |2a, 2b\rangle + \dots \quad (5)$$

2.2 Entanglement by Path Identity

An important element in the development of quantum optical experiments is the concept of entanglement by path identity. This is mostly easily demonstrated by examining the original experiment developed by Zou, Wang, and Mandel [16, 25]. Using two crystals which produce photon pairs, the paths of of one pair from each crystals is overlapped (as is seen in Fig. 2. This procedure removes the “which-path” information from the resulting photon detected using detector d. This procedure creates a state:

$$|\psi\rangle = \frac{1}{\sqrt{2}}(|a, d\rangle + |c, d\rangle) = 1/\sqrt{2}(|a\rangle + |c\rangle)|d\rangle. \quad (6)$$

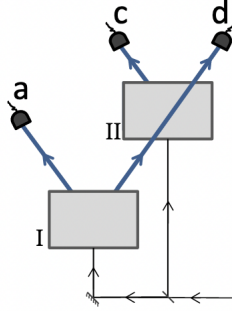


Figure 2: Experimental setup for path entanglement generation of $|\psi\rangle = 1/\sqrt{2}(|a\rangle + |c\rangle)|d\rangle$. Crystal I and II are pumped by a laser. If we can not distinguish in which crystal the photons were created, we make a state consisting of one photon in path d and another photon in coherent superposition of path a and c. Image taken from [12].

In recent years, entanglement by path identity has developed significantly and has potential for many applications, including new types of imaging technology [9]. However, the simple ability to generate entanglement, demonstrated in Eq. 6, will suffice for the experiments we examine.

3 Realization of Quantum Experiments in a Silicon Chip

Entanglement by path-identity may seem like far-off tools that can only be implemented using large laboratory experiments under hermetic conditions similar to current quantum computing technology. However, there are now millimeter-scale silicon chips capable of using this phenomenon.

In particular, Feng et al.[6] have successfully developed silicon chips capable of creating experimental setups similar to those shown in Fig. 4 using entanglement by path identity. A depiction of the experimental setup is given in Fig. 3. This leads to resulting states expressed as

$$\begin{aligned}
 |\psi\rangle = & g^2 (|2a, 2b, 0, 0\rangle + |2a, 0, 2c, 0\rangle + e^{2i\theta}|0, 2b, 0, 2d\rangle \\
 & + |0, 0, 2c, 2d\rangle) + \sqrt{2}g^2 (|2a, b, c, 0\rangle + e^{i\theta}|a, 2b, 0, d\rangle \\
 & + |a, 0, 2c, d\rangle + e^{i\theta}|0, b, c, 2d\rangle) + g^2 (1 + e^{i\theta}) |a, b, c, d\rangle.
 \end{aligned} \tag{7}$$

Postselecting this state for fourfold coincidence yields

$$g^2 (1 + e^{i\theta}) |a, b, c, d\rangle. \tag{8}$$

where θ stands for the angle of the phase shifter gate shown in Fig. 3. This phase tuning gives the chip the ability to carefully modulate the number of photon pairs produced (this ability is referred to as frustrated down conversion). The addition of the phase shifter and the resulting term in equation 8 give a natural intuition for the addition of complex weights which we will introduce in Sec. 5. Further, the fact that this experiment uses spatially separated sources entangled using path identity opens the possibility for new experiments on non-locality as well as many other practical applications [6].

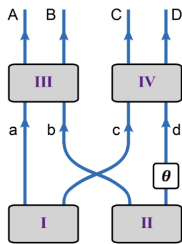


Figure 3: Abstract depiction of four photon experiment developed on a silicon chip. Figure copied from [6].

4 A Very Brief Introduction to Multidimensional Entanglement

In order to understand quantum experiments, we must understand their output. In recent years, the possibility of a much richer environment of quantum states has emerged. We will focus on what is called a GHZ (Greenberger-Horne-Zeilinger state). For a two-dimensional (qubit system) it can be written as

$$|\text{GHZ}\rangle = \frac{|0\rangle^{\otimes M} + |1\rangle^{\otimes M}}{\sqrt{2}}. \quad (9)$$

More generally, for a d -dimensional m -partite quantum system we have

$$|\psi\rangle = \frac{1}{\sqrt{d}} \sum_{i=0}^{d-1} |i, i, i, \dots\rangle. \quad (10)$$

m times

GHZ states have applications in the foundations of quantum mechanics, where they can be used to develop experiments to disprove local hidden variable theories of quantum mechanics [4].

GHZ states are symmetrically and maximally entangled system (i.e each part of the system is equivalently entangled to any other part of the system).

To formalize this notion, we need to introduce the concept of a Schmidt-rank vector. Given any state w in bipartite quantum system $H_1 \otimes H_2$, we can form the Schmidt decomposition:

$$w = \sum_{i=1}^m \alpha_i u_i \otimes v_i \quad (11)$$

where u_i and v_i are orthonormal basis vectors. The coefficients α_i are real coefficients s.t $\sum_{i=1}^m \alpha_i^2 = 1$. The number of terms in the decomposition is the Schmidt rank. We can generalize this process to higher-partite systems. For example, given a tripartite quantum system. $|\psi\rangle \in H_A \otimes H_B \otimes H_C$

$$\begin{cases} \hat{\rho}_A = \text{Tr}_B(|\psi\rangle\langle\psi|) \\ \hat{\rho}_B = \text{Tr}_A(|\psi\rangle\langle\psi|) \\ \hat{\rho}_C = \text{Tr}_{AB}(|\psi\rangle\langle\psi|) \end{cases} \quad (12)$$

Calculating the Schmidt rank for each of these subsystem will give us the Schmidt-rank vector. For example, the Schmidt rank vector of the 3-partite 3-dimensional GHZ state, $\frac{1}{\sqrt{3}}|0, 0, 0\rangle + |1, 1, 1\rangle + |2, 2, 2\rangle$, is (3,3,3).

Schmidt-rank vectors will help characterize the range of multidimensional states quantum experiments developed on computational systems can generate. It is interesting to note that the dimension of elements in the Schmidt rank vector indicates the “power” of the given state in the sense that the dimensionality of the state can easily be decreased but cannot be increased using LOCC (Local Operations and Classical Communication), that is, we can easily measure states but we cannot entangle two states using local operations alone[8].

5 Quantum Experiments to Graph Correspondence

In order to use automated design algorithm, we must first convert potential quantum experiments to machine and preferably human readable form. A remarkable solution method to this issue is the representation of quantum experiments as graphs. Experiments using quantum entanglement by path identity as well as linear optics can be represented using undirected graphs [8]. Each crystal in a given experiment can be represented by an edge in a graph and the OAM mode numbers of the generated photon are represented by the color of this edge. Each path can be represented as a vertex. A concise overview is given below.

Quantum Experiment	Graph Theory
Optical Setup with Crystals	undirected Graph (V,E)
Crystals	Edges E
Optical Paths	Vertices V
n-fold coincidence	perfect matching
#(terms in quantum state)	#(perfect matching)
maximal dimension of photon	degree of vertex
n-photon d-dimensional GHZ state	n-vertex graph with d-disjoint perfect matchings

Table 1: Original analog between quantum experiments and graphs. Reproduced from [12].

This correspondence was originally developed for entanglement by path identity but can easily be adapted to traditional linear optical experiments as well.

Linear optical quantum experiments	Graph theory
Quantum photonic setup including linear optical elements and nonlinear crystals	Complex weighted undirected graph
Optical output path	Vertex set S
Photonic modes in optical output path	Vertices in vertex set S
Mode numbers	Labels of the vertices
Photon pair correlation	Edges
Phase between photonic modes	Color of the edges
Amplitude of photonic modes	Width of the edges
n-fold coincidence	Perfect matching
#(terms in quantum state)	#(perfect matchings)

Table 2: Correspondence between quantum experiments and graphs. Reproduced from [8].

A matching M of a graph $G=(V,E)$ is a set of edges such that no two edges share the same vertices. A vertex is said to be matched if it is part of one of the edges in the matching. A perfect matching is a matching such that all vertex in a graph G are matched. Each perfect matching correspond to a term in the resulting state. For example, if we are postselecting on four-fold coincidence with the experiment in Fig. 4, any four-fold coincidence results from the detection of a photon in each path (a,b,c,d). Furthermore, each crystal can only generate photons in two paths using SPDC. While

entanglement by path identity and postselection entail that terms that result from two edges sharing the same vertex will not be considered (i.e using just crystals I and III would not result in fourfold coincidence).

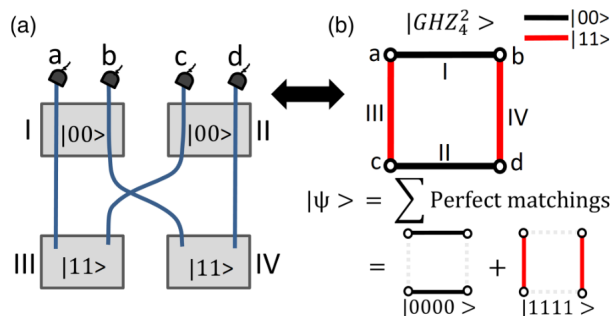


Figure 4: Depiction of an experiment using entanglement by path identity to generate 2-dimensional 4-particle GHZ state while post selecting on fourfold coincidence. Figure reproduce from [8].

The correspondence between quantum experiments and graphs will not only prove practical for computational automation but is also a very conceptually useful perspective to think about quantum optical experiments. In particular, graphs can effectively illustrate what quantum states can and cannot be created using entanglement by path identity [12]. A good example of the benefit of this approach can be seen in the design of quantum experiments for GHZ states.

A GHZ state is only available when all perfect matching in the experiment graph are disjoint (i.e every edge only appears in one perfect matching[12]). If this is not the case, additional terms, dubbed “maverick” terms, are present. Therefore, the question of what d -dimensional GHZ states can be created is transfigured into the question “which undirected graphs exist with d -perfect matchings which are all disjoint?” [12].

Using only path entanglement we can generate any 2-dimensional n -particle GHZ state by simply adding more vertices to the graph shown in Fig. 4. This is possible because any cyclic graph with more than three vertices C_n has two disjoint perfect matchings. For a complete graph K_n (where $n \geq 4$) there exists 3 disjoint perfect matchings; therefore, we can create any 3-dimensional n -particle GHZ state. However, it is not possible to form a graph of more than 3 disjoint perfect matchings, and hence higher-dimensional n -particle GHZ states are not possible using these methods. The proof of these assertion requires some additional graph theory and is included in the references [1].

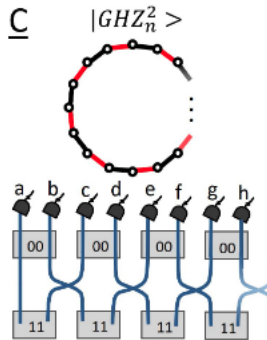


Figure 5: Graph corresponding to arbitrary n particle 2 dimensional GHZ state along with Crystal and path setup. Figure taken from [8].

6 Computational Complexity and Perfect-Matching

Using the power of the graph approach we can gain insight into the computational complexity of simulating quantum optical experiments on classical computers. Consider an experiment referred to as “the crystal network” [8] consisting of N nonlinear crystals and M optical output paths. First, n of N crystals are pumped to produce photon pairs. The photons are entangled using path identity and the $2n$ fold coincidence is measured. The output state of this setup is determined by the sum of perfect matchings in the complex weighted graph representing the experimental setup. In general the number of perfect matchings in a graph is given by the hafnian of the graph’s adjacency matrix. For a $2n \times 2n$ matrix, A , the hafnian is given by

$$\text{haf}(A) = \frac{1}{n!2^n} \sum_{\sigma \in S_{2n}} \prod_{j=1}^n A_{\sigma(2j-1), \sigma(2j)}. \quad (13)$$

The most efficient algorithm to determine the hafnian of arbitrary $n \times n$ matrix runs in $O(n^3 2^{n/2})$. In fact, counting the number of perfect matchings in an arbitrary graph is $P\#$ complete. If you are acquainted with computational complexity theory, a given $P\#$ problem measures the number of accepting paths of a polynomial-time nondeterministic turing machine. $P\#$ problems are at least as hard as NP-complete problems[24].

6.1 Comparison with Boson Sampling

The concept of crystal networks offers a promising direction to explore quantum supremacy. However, the idea of using photon counting to look at com-

putational complexity and quantum supremacy is not a new one. In recent years, boson sampling has emerged as a promising method for demonstrating quantum advantage [8]. Boson sampling works by pumping n SPDC crystals, which are fed into an optical setup consisting of m input and output paths. However, boson sampling is based on a completely passive linear optical network where photon states are transformed using a multi-photon version of the Hong-Ou-Mandel effect. The count-rate for the original boson sampling experiment is

$$R_{BS} \approx p^n, \quad (14)$$

where p is the probability of SPDC emission. This count rate is quite low. However, this count rate was exponentially improved using Scattershot and Gaussian boson sampling [22, 17]. These methods yield a count rate of

$$R_{SS} \approx \binom{m}{n} p^n (1-p)^{m-n}. \quad (15)$$

However, the count rate of a crystal network setup has the potential to be much higher than even Scattershot or Gaussian boson sampling. For m^2 crystals creating photon pairs the count rate is given by

$$R_{CN} \approx \binom{m}{n}^2 n! p^n (1-p)^{m^2-n}. \quad (16)$$

This yields a magnification on the order of $n!$ in the count-rate compared with Scattershot/Gaussian boson sampling. Nevertheless, this result does not factor in real-world imperfections which might affect the count rate. A full investigation of the real-world effects relevant to the crystal network approach is needed to make a proper comparison with boson sampling [8].

To see how this magnification arises consider 4-fold coincidence in the bipartite graph shown in Fig. 6. We are considering a bipartite graph because the hafnian of a bipartite graph is the permanent of the graph's adjacency matrix. We would like to make a fair comparison between the two methods and boson sampling measures the permanent. There are two sets of edges a, c, e and b, d, f . Any four-fold coincidence, for example, $abcd$, will need to select two edges from each set leading to $\binom{3}{2} \cdot \binom{3}{2}$ combinations. Further, each detection results from $2!$ crystals i.e., for the coincidence $(abcd)$ we can choose either crystal I or II but then we must choose crystal IV.

In general, for m^2 crystals (edges) and $2n$ -fold coincidence (n vertices from each side of the bipartite graph) we have $\left(\binom{m}{n}\right)^2$ $2n$ -vertex pairs to choose from (there are roughly m vertices on each side). In addition, for each vertex set chosen, there are also $\approx n!$ crystals to choose from. The intuition behind

the $n!$ factor is somewhat more complicated. The number of perfect matching for n vertices is bounded above by the number of perfect matchings of an n -vertex complete graph given by $\frac{n!}{(2!)^{n/2}(n/2)!}$ [12]. The probability factors are due to the fact that for any $2n$ -fold coincidence n crystals must fire and $(m^2 - n)$ must not, which accounts for the $p^n(1 - p)^{m^2 - n}$ factor.

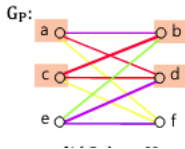


Figure 6: Depiction of a bipartite experiment graph. Image taken from [8].

7 MELVIN

We now have all the concepts in place to look at the MELVIN quantum experiment design system [14]. We will only cover this system briefly because newer frameworks, notably Theseus, have superseded MELVIN in many metrics. MELVIN is based on manipulating symbolic algebra where abstract functions are used to represent quantum experiment components. For example, a quantum beam splitter is represented by a function,

$$\text{BS}[\psi, a, b] = \psi \Leftarrow \begin{cases} a[\ell] \rightarrow \frac{1}{\sqrt{2}}(b[\ell] + i \cdot a[-\ell]) \\ b[\ell] \rightarrow \frac{1}{\sqrt{2}}(a[\ell] + i \cdot b[-\ell]) \end{cases} \quad (17)$$

where ℓ is the OAM mode. Reflection is represented by

$$\text{Reflection}[\psi, a] = \psi \Leftarrow \begin{cases} a[\ell, H] \rightarrow -i \cdot a[-\ell, H] \\ a[\ell, V] \rightarrow i \cdot a[-\ell, V] \end{cases} \quad (18)$$

where H, V stand for horizontal and vertical polarization respectively. Krenn et al. use these transformations to build an optical setup. After the state is formed, it is analyzed to determine its properties, including its Schmidt-rank vector. If the state satisfies a predetermined property, for example it forms a GHZ state, the optical setup is simplified. Furthermore, if the solution is deemed useful, it can be saved as another tool in the algorithms toolbox of transformations/components.

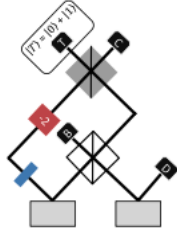


Figure 7: Experimental design for the creation of a 3-dimensional 3-partite GHZ state developed by the MELVIN algorithm. On detection (measurement) of $|0\rangle + |1\rangle$ the state is known to be $|\psi\rangle = \sqrt{13}|0, 0, 0\rangle + |1, 1, 1\rangle + |2, 2, 2\rangle$. The central diamonds are beam splitters, the -2 stands for a OAM hologram operation which shifts down the optical mode. Figure reproduced from [14].

MELVIN is able to generate a remarkable range of states including the first implementation of a high-dimensional GHZ state. The table in Fig. 8 shows the states generated using MELVIN after several months of CPU time [14].

Possible experimental implementations for SRV(A,B,C) states

2,2,2	3,2,2	4,2,2	5,2,2	6,2,2	7,2,2	8,2,2	9,2,2	10,2,2
3,3,2	4,3,2	5,3,2	6,3,2	7,3,2	8,3,2	9,3,2	10,3,2	
3,3,3	4,3,3	5,3,3	6,3,3	7,3,3	8,3,3	9,3,3	10,3,3	
4,4,2	5,4,2	6,4,2	7,4,2	8,4,2	9,4,2	10,4,2		
4,4,3	5,4,3	6,4,3	7,4,3	8,4,3	9,4,3	10,4,3		
4,4,4	5,4,4	6,4,4	7,4,4	8,4,4	9,4,4	10,4,4		
5,5,2	6,5,2	7,5,2	8,5,2	9,5,2	10,5,2			
5,5,3	6,5,3	7,5,3	8,5,3	9,5,3	10,5,3			
5,5,4	6,5,4	7,5,4	8,5,4	9,5,4	10,5,4			
5,5,5	6,5,5	7,5,5	8,5,5	9,5,5	10,5,5			
6,6,2	7,6,2	8,6,2	9,6,2	10,6,2				
6,6,3	7,6,3	8,6,3	9,6,3	10,6,3				
6,6,4	7,6,4	8,6,4	9,6,4	10,6,4				
6,6,5	7,6,5	8,6,5	9,6,5	10,6,5				
6,6,6	7,6,6	8,6,6	9,6,6	10,6,6				
7,7,2	8,7,2	9,7,2	10,7,2					
7,7,3	8,7,3	9,7,3	10,7,3					
7,7,4	8,7,4	9,7,4	10,7,4					
7,7,5	8,7,5	9,7,5	10,7,5					
7,7,6	8,7,6	9,7,6	10,7,6					
7,7,7	8,7,7	9,7,7	10,7,7					
8,8,2	9,8,2	10,8,2						
8,8,3	9,8,3	10,8,3						
8,8,4	9,8,4	10,8,4						
8,8,5	9,8,5	10,8,5						
8,8,6	9,8,6	10,8,6						
8,8,7	9,8,7	10,8,7						
8,8,8	9,8,8	10,8,8						
9,9,2	10,9,2							
9,9,3	10,9,3							
9,9,4	10,9,4							

■ possible implementations found by Melvin
■ additional implementations found using graph theory
■ not possible based on graph theory
■ not possible

Figure 8: Table of Schmidt-rank vector states reproduced from [8]. The states in green were generated using the MELVIN framework over a period of months. The States in red cannot be generated for graph theoretical reasons (see Sec 9). Experimental configurations have been found for the light green states (MELVIN cannot identify these setups). States in black cannot exist because of theoretical limitations (see 9). Note, the table is slightly in error the states (10,7,3) and (10,7,4) can be produced while the states (10,7,2) and (8,4,3) cannot (see Sec 11.3).

8 Theseus

The MELVIN system is an impressive attempt at developing novel experiments. However, the system can be remarkably slow and does not directly take into account two crucial insights that we have learned about quantum experiments. First, the algorithm does not explicitly exploit entanglement by path identity. Second, the algorithm does not utilize the graph nature of quantum experiments mentioned earlier. For these reasons Krenn et al., 2021, developed another system called Theseus [13], which is built around exploiting these two new insights in quantum experiment development.

Theseus relies on topological optimization of quantum experimental graphs. Let us consider what this function should be, like any optimization algorithm, we need to first find a suitable function to optimize. Since we are interested

in state generation, we should find an appropriate function to measure the distance between the desired state and the result produced by the experiment. This is measured by looking at the fidelity between the desired and produced state. But how can we find this fidelity? Theseus's main benefits lies in its graph abstraction. However, under the hood Theseus is a completely symbolic system. In order to understand the output state generate by the system, we must first understand the symbolic computation as well. Any quantum experiment/graph can be expressed as a single operator on a vacuum state called the weight function. The weight function is a generalization of the Taylor expansion of the SPDC operator we saw earlier (see 4). In abstract terms, this process is represented by

$$|\Psi\rangle = \Phi(\omega)|vac\rangle. \quad (19)$$

To understand how this weight function is constructed, we look at the weight function of the 2-dimensional 4-partite GHZ state, $|GHZ\rangle = 1/\sqrt{2}(|0, 0, 0, 0\rangle + |1, 1, 1, 1\rangle)_{a-d}$.

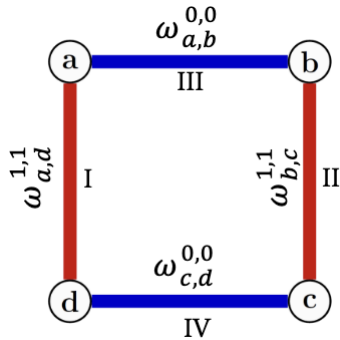


Figure 9: Diagram of four crystal experimental setup with four complex-weighted paths. If all weights are equal this crystal structure produces the 4-qubit GHZ state $|GHZ\rangle = 1/\sqrt{2}(|0, 0, 0, 0\rangle + |1, 1, 1, 1\rangle)_{a-d}$. Diagram taken from [13].

The weight function for the experimental setup in Fig. 9 is

$$\begin{aligned} \Phi(\omega) \approx \sum_m 1/m! \left(\sum_{E(G)} \omega(E) x^\dagger(E) y^\dagger(E) \right)^m = \\ \sum_m 1/m! \left(\omega_{a,b}^{0,0} a_0^\dagger b_0^\dagger + \omega_{c,d}^{0,0} c_0^\dagger d_0^\dagger + \omega_{a,c}^{1,1} a_1^\dagger c_1^\dagger + \omega_{b,d}^{1,1} b_1^\dagger d_1^\dagger \right)^m, \quad (20) \end{aligned}$$

where a_n^\dagger is the creation of operator for one photon in path a with OAM mode n. While $\omega_{a,b}^{n,m}$ are complex weights corresponding to the creation of OAM n and m mode photons in path a and b respectively.

Doing the necessary expansion to $m = 2$ and postselecting on fourfold coincidence yields

$$|\Psi\rangle = \Phi(\omega)|vac\rangle \approx (\omega_{a,b}^{0,0} \cdot \omega_{c,d}^{0,0}|0, 0, 0, 0\rangle + \omega_{a,c}^{1,1} \cdot \omega_{b,d}^{1,1}|1, 1, 1, 1\rangle). \quad (21)$$

The fidelity is given by the projection of this output state on the desired GHZ state, which is

$$\begin{aligned} & \frac{1}{\sqrt{2}}\langle 0, 0, 0, 0| + \langle 1, 1, 1, 1|\Phi(\omega)|vac\rangle \\ &= \langle 0, 0, 0, 0|\Phi(\omega)|vac\rangle + \langle 1, 1, 1, 1|\Phi(\omega)|vac\rangle \\ & \quad = \omega_{a,b}^{0,0} \cdot \omega_{c,d}^{0,0} + \omega_{a,c}^{1,1} \cdot \omega_{b,d}^{1,1} \end{aligned} \quad (22)$$

$$F(\omega) = \frac{|\omega_{a,b}^{0,0} \cdot \omega_{c,d}^{0,0} + \omega_{a,c}^{1,1} \cdot \omega_{b,d}^{1,1}|^2}{2 \cdot N(\omega)^2} \quad (23)$$

where $N(\omega)$ is the normalization factor equal to

$$N(\omega) = \sqrt{|\omega_{a,b}^{0,0} \cdot \omega_{c,d}^{0,0}|^2 + |\omega_{a,c}^{1,1} \cdot \omega_{b,d}^{1,1}|^2}. \quad (24)$$

However, $F(\omega)$ is not exactly the function that we would like to optimize. We want to preference those experiments with smaller edge weights. Therefore, we will include an L1 regularization term. The strength of this regularization is determined by $\alpha < 1$, which is set by default to 1/2 [13]. Therefore, our final loss function is

$$L(\omega) = [1 - F(\omega)] + \alpha \cdot |\omega|_1. \quad (25)$$

Theseus's algorithm works by starting with a fully connected multigraph between paths/vertices (multiedges corresponding to multiple pairs of mode numbers). The fidelity is optimized using two distinct processes. Continuous edge weights are optimized using BFGS (Broyden-Fletcher-Goldfarb-Shanno algorithm). If after BFGS the computed fidelity exceeds a fidelity limit (F_{limit} is set by default to 0.95) then Theseus looks at the sum of weights. If the sum of weights is below the weight limit then an edge is removed from the graph (this can either be done randomly or by removing the least weighted edge) and the process repeats until the iteration limit is reached. However, if the fidelity and weight condition are not met, the same graph is optimized again

with the number of iterations reset as well as the weight starting conditions. [13].

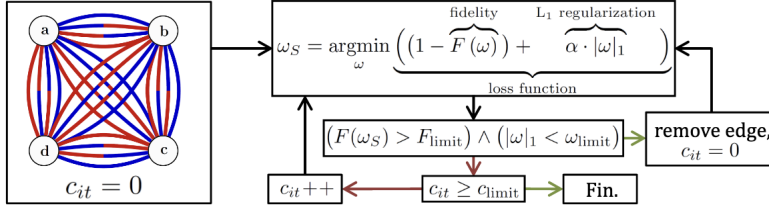


Figure 10: Visual depiction of Theseus’s algorithm. Initial graph has all possible edges with all possible mode numbers. The graph’s colored edges correspond to different mode numbers. Reproduced from [13].

8.1 Theseus’s Inventions: Heralded Bell and GHZ states

An impressive result of the Theseus system is the heralded 3 dimensional Bell and GHZ state. Heralded states are a useful improvement over traditional state generation where states are generated at random times which mean that the generation of an entangled state is not known until it is measured. Heralded states are “heralded” using trigger detection which allows them to be used in a broader set of event-ready quantum experiments. Heralded versions of two-dimensional Bell states are well known. Remarkably, Theseus is able to develop a new design for heralded 3-dimensional Bell states as well. Theseus develops this experimental apparatus using a new conceptual idea of destructively interfere the vacuum which solves the common issue in heralded states where triggers herald the vacuum term much more often than the intended state [13].

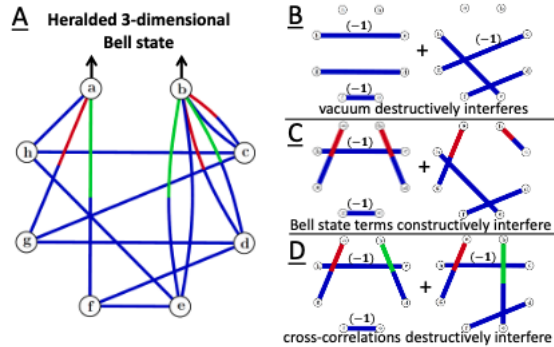


Figure 11: Panel A shows Theseus’s design of heralded 3-dimensional Bell state. Panel B shows how the design uses destructive interference on the vacuum. Diagram taken from [13].

8.2 Comparison of Theseus and MELVIN

As a benchmark to compare the abilities of Theseus and MELVIN we will look at states with different Schmidt-rank vectors. We will focus on maximally entangled states. Further stipulating that a state with Schmidt rank vector (A,B,C) has A terms where $A \geq B \geq C$. These are a good set of states to easily visualize entanglement in the computational basis [8]. We will refer to such state as $SRV(A,B,C)$ states from now on.

Theseus is capable of generating many states that were not possible with the MELVIN system. Theseus is also orders of magnitude faster than MELVIN. MELVIN takes around 150 CPU hours to find 51 of 81 possible $SRV(A,B,C)$ with $A \leq 10$ (see Figure 8). Theseus identifies 76 of the possible $SRV(A,B,C)$ states within 2hrs CPU time [13].

Further, Theseus is able to generate graph representations of its results which are much more easily interpreted than MELVIN’s result which given long sequences of function operations comparable to Eq. 17.

However, when we ran Theseus ourselves, the time it took the algorithm to discover a given $SRV(A,B,C)$ state increased quite dramatically with A, B , and C . For instance, state $(10,8,5)$ takes 5991 iterations, while no experimental setup for $(10,7,6)$ was found even after 10,000 iterations. In comparison, for $A = 2, 3$ one iteration sufficed to discover all possible states. We give a depiction of our analysis in Fig. 12.

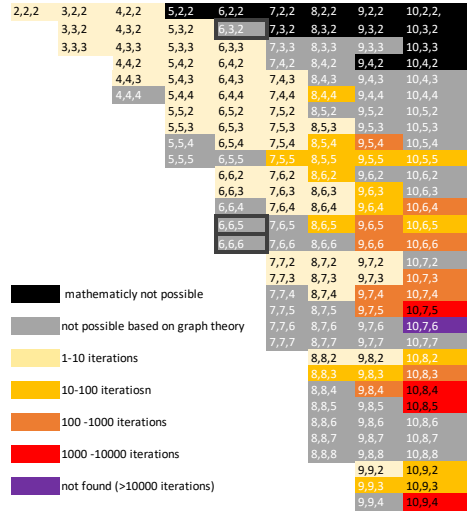


Figure 12: SRV(A,B,C) states discovered by Theseus colored by number of iterations taken to discover the state. Computation run by author using code from the [Theseus Github Repo](#).

9 What States Cannot be Produced?

9.1 Proof of Rank Limits

Not all Schmidt-rank vectors are possible. Here we present a proof of one of the most basic rank vector bounds using entropy inequalities taken from Huber et al. [10]. The author has developed another proof of this proposition in Sec. 11.2 which relies on simple combinatorics.

For a 3-partite entangled state described by a Schmidt-rank vector (r_A, r_B, r_C) , if we suppose without loss of generality that $r_A \geq r_B \geq r_C$ then

$$r_A \leq r_B r_C. \tag{26}$$

This limitation is the reason behind the black states in 8.

Proof: The proof follows from subadditivity of the Rényi 0-entropy [10].

$$S_0(\rho_{AB}) \leq S_0(\rho_A) + S_0(\rho_B) \quad (27)$$

[15]. The Rényi- α entropy is given by the following formula.

$$\mathcal{S}_\alpha(\rho_A) = \frac{1}{1-\alpha} \log \text{tr}(\rho_A^\alpha). \quad (28)$$

Exponentiation of the subadditivity condition of Rényi-0 entropy leads to

$$\text{tr}(\rho_{BC}^0) \leq \text{tr}(\rho_B^0)\text{tr}(\rho_C^0). \quad (29)$$

The Rényi 0-entropy is equivalent to rank for density matrices and the rank of ρ_{BC} is equivalent to that of ρ_A [10]. For those not familiar, when we write a given density matrix in its spectral decomposition, $\rho = \sum_i \lambda_i |i\rangle\langle i|$, the Rényi 0-entropy is $\sum_i \log(\lambda_i^0)$.

9.2 Graph Bounds on State Creation

Equation 26 is a bound that holds for any n-particle quantum system [3]. However, there are further bounds on state creation in particular quantum experiments that can be demonstrated using graph theory. We illustrate one such bound derive by Gu et al. which solves an open question raised 3 years previously [8] (more recent open question are listed here [19]). We also provide a simplification of this result and our own alternative proof of this bound in Sec.11.4. This bound establishes limits on SRV(A,B,C) states created by 3 particle entanglement and one trigger photon. Such experiments are the simplest way to generate heralded SRV(A,B,C) states (a 3-vertex graph has no perfect matching). In addition, the states generated in this process have been extensively studied experimentally [18] [5] and with computer-based design [21] [14].

The limit of SRV(A,B,C) generation using 3 particle entanglement and one trigger is given by

$$1 + \min(1 + (A - B), C) + \min(1 + (A - C), B - 1) \geq A. \quad (30)$$

9.3 Derivation of Graph Bounds on State Creation

Here we present a derivation of the above equation (Eq. 30) presented in [8]. We have tried to recapitulate and fill in the derivation presented in [8] as

best as possible. However, some parts are not as rigorous as we would like. We refer the reader to 11.4 for an alternative derivation.

This derivation relies quite heavily on intuition for the kinds of state that can be produced by a given graph. We refer the reader to figures 16, 14, 15 to gain insight. Two important concepts to remember are every edge in each perfect matching can have 2 mode numbers and each perfect matching generates one term in the resulting state.

As a reminder, our experimental set-up consists of 3 particles a,b,c and a trigger t (the trigger has a constant mode number). The dimensionality of each particle a,b,c is given by A,B,C, respectively. We assume without loss of generality that $(A \geq B \geq C)$. We refer to the collection of perfect matchings with edges $E_{t,a}, E_{t,b}, E_{t,c}$ respectively as graphs I, II, and III (see Fig 13). It is also important to note a trick that we will use throughout the rest of the essay.

Remark (repeat-mode rule). *No two terms can have the same two mode numbers or the dimension of the state will be reduced $|0\rangle_a|0,0\rangle_{b,c} + |1\rangle_a|0,0\rangle_{b,c} = (|0\rangle + |1\rangle)_a|0,0\rangle$.*

We will construct the inequality in Eq. 30 by looking at the maximum number of terms that can be produced using the given setup and mode/term restrictions. This maximum must be greater than A (which is the total number of terms). Every term in the end state is the result of a perfect matching in the experiment graph. However, for K_4 there are only 3 perfect matchings [12]. Yet, with four vertices states like SRV(6,5,3) exist which involve at least 6 terms. To get around this limitation, we use multiedges. For every perfect matching one edge is connected to the trigger vertex t. Why cant we form a multi-edge with the trigger? Since the trigger has a constant mode number, a multiedge for example between b and t in graph II, would lead two terms with the same a and b mode and a violation of the repeat-mode rule.

Let's prove the inequality term by term in Eq. 30. First, +1, consider graph I with edge $E_{t,a}$. Since there cannot be multiple terms in the output state with the same a-mode number, we cannot form a multi-edge between t and a or between b and c. Therefore, there is only one term we can form using graph I.

$\min(1 + (A - B), C)$ term:

Now if we consider graph II, all terms generated using this graph have the same b-mode number. Photon b in our SRV(A,B,C) state has B terms with B different mode numbers. We can have at maximum (A-B)+1 terms

with the same b-mode number and still have B different mode numbers in total. Therefore, we can make at maximum $(A-B)+1$ terms using graph II (all terms generated using graph II have the same b-mode).

Note, however, that it is not always possible to create $(A-B)+1$ repeat terms because for each repeat b-mode term we must have a different c-mode (repeated-mode rule). Therefore, the number of terms with the same b-mode number is limited by C. Finally, the maximum number of terms that can be generated using graph II is $\min(1 + (A - B), C)$.

$\min(1 + (A - C), B - 1)$ term :

For graph III we can apply the same method as for graph II. As before, every term generated using graph III must have the same c-mode number. Given that we have C different mode numbers and A terms in total, we can form at maximum $(A - C) + 1$ terms with the same mode number.

The maximum number of terms generated by graph III is limited by the number of usable B-modes. All terms created using graph III must have different b-mode numbers, or we end up generating terms violating the repeat-mode rule. Since we used one b-mode in the perfect matching in graph I we can create at maximum B-1 terms with different b-modes using graph III. Therefore, the maximum number of terms that can be created using graph III is $\min(1 + (A - C), B - 1)$.

The sum of the maximum number of possible terms generated from graphs I, II, and III must be greater than or equal to the number of actual terms. This condition gives the desired result Eq. 30.

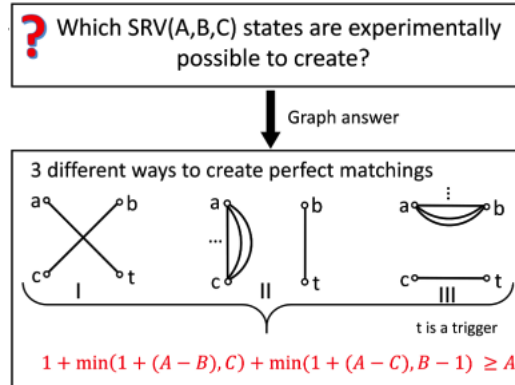


Figure 13: Illustration of the perfect matching that exist for 3 entangled particles and one trigger. The leftmost figure with edge $E_{t,a}$ is referred to as graph I, graph II contains edge $E_{t,b}$, while the rightmost graph with edge $E_{t,c}$ is referred to as graph III. Figure modified by author from original taken from [8].

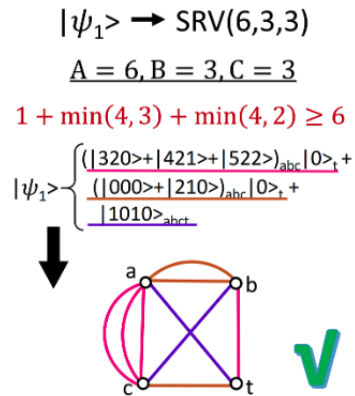


Figure 14: Example construction of SRV(6,3,3) state. Edge color correspond to disjoint perfect matchings. This color-scheme is different from the edges color used to signify OAM mode (see Fig. 16). Each edge/crystal in the diagram can produce multiple OAM modes. Image taken from [8].

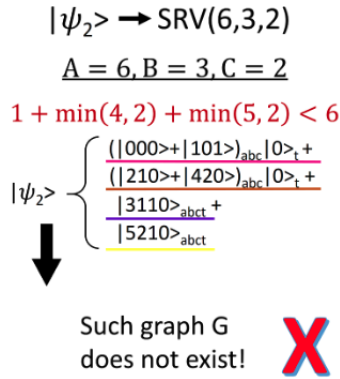


Figure 15: Illustration of a state not possible given graph limitations. We note that looking at only the b-modes in the state gives 001212. This pattern violates the statement in step 1 of Sec. 11.4. Image taken from [8].

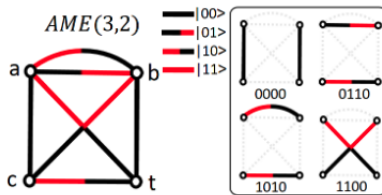


Figure 16: Depiction of the design for an $\text{AME}(3,2)$ (absolutely maximally entangled state). The resulting state is $|\phi\rangle_{abct} = \frac{1}{2}(|000\rangle + |011\rangle + |101\rangle + |110\rangle)|0\rangle$. Notice how you can see the resulting states generated. Image taken from [8].

10 Conclusion and Further Directions

We have discussed how automated systems can design quantum experiments and how these experiments work at a theoretical and experimental level. We have used this framework to conceptualize how an algorithm can be capable of finding new insights into quantum optical design. In this essay we have tried to give the core insights used to explore these methods. Nevertheless, we have not addressed many things. We have neglected to cover the generalization of the graph model to hypergraphs which includes the production of more than two photons from a single source [7].

We have also neglected the extension of Theseus to quantum computers. It is possible to use quantum hardware to optimize quantum computa-

tional design by converting quantum optical experiments into quantum circuits [11]. The potential to model quantum experiments using circuit-based quantum computing opens the door to apply many methods developed in hybrid-quantum classical computation to the development of quantum optical systems.

Further, there remain open questions about Theseus itself. What does the optimization landscape for Theseus look like (How would noise affect this landscape)? For higher-dimensional states does Theseus runs into Barren plateau issues which are major problem for quantum neural networks [20]. Such issues might pose problems for the expansion of Theseus as a general tool for experimental design. Moreover, in all our experiments we optimized over the number and weight of edges, optimizing over vertices could improve the versatility of Theseus.

In relation to states producible by graphs, open questions can be found in [19]. Further, in depth comparison of the crystal network approach to boson sampling in particular regards to noise remains open [8].

Given the ability of Theseus to explore 3 dimensional entanglement the extension to four dimensional entanglement could be particularly lucrative. The universe of many-partite Hilbert space is still unexplored. For $n = 4$ parts, there remains a conjecture on the bound of Schmidt-rank vectors [3]. Given the capability of Theseus to generate many different kinds of multipartite states, it would be insightful to see if Theseus can support or invalidate this conjecture. Moreover, for any higher number of parts the landscape of available quantum states including any further theoretical bounds are unknown. Theseus and the techniques used in this essay could act as a telescope into this world of these quantum states.

Nature has many discoveries to unravel. We hope that this essay has given a glimpse of the ocean beyond the shore and the potential of computers to help us see the horizon. Perhaps the scientist of the future will stand on the shoulders of a new kind of giant.

11 Appendix: New Derivations

11.1 Summary of New Results

The following results are derived by the author and are not present in any of the references to the best of the author’s knowledge. However, it should be mentioned that Gu et al.,2019,[8] suggests that Eq. 26 is combinatorial but does not prove this statement and cites the proof discussed in Sec. 9 from [10].“New derivation of $A \leq BC$ ” presents the combinatorial proof to

Eq. 26 (derived by the author) which offers a much simpler derivation. The section, “New Insight into SRV(A,B,C) State Creation Bounds”, introduces a new simplification of the bounds presented in Sec. 9.2. Using this new elucidation, we are able to identify errors in the state classification presented in Fig. 8 as well as offer a new derivation of equation 30 presented in section 11.4.

11.2 New Derivation $A \leq BC$

Given a state with a Schmidt-rank vector (A,B,C), particles A,B, and C must have A,B and C different mode numbers. Further, no two terms can share two a/b/c mode numbers (repeat-mode lemma). Given that there are A terms, the minimum number of terms with the same B number is (A/B) none of the terms in this group (i.e group with constant b mode) can have the same c mode. Therefore, by the pigeonhole principle, $C \geq (A/B)$, which yields the desired result.

11.3 New Insight into SRV(A,B,C) State Creation Bounds

Equation 30 is quite complicated. The author has found a novel simplification of this equation using Mathematica which can be written as

$$A - B \leq C \leq A - B + 3. \quad (31)$$

This offers a clearer and more suggestive result. For example, we can see how the classification of (8,4,3), (10,7,2),(10,7,3),(10,7,4) are erroneous in Fig. 8 originally presented in [8]. Further, the lower bound is given by $A - B$ which is the number of non-independent b modes in the first proof. We will use these hints to develop a second proof. For a direct proof of this result from Eq. 30. The interested reader can derive the result by dividing the original formula Eq. 30 into cases and proving the result for each of these cases (i.e there are four cases case one of these is $1 + (A - B) \leq C$ and $1 + (A - C) \leq B - 1$).

11.4 New Proof of Graph Bounds on State Creation

We take two concepts from the original proof: the repeat-mode rule, as well as assuming that the matchings present in graphs I,II, and III (shown in Fig. 13) are the only matchings. We define the new concept of a mode set. For a given state say ,SRV(4,2,2) = $\frac{1}{2}|000\rangle + |101\rangle + |210\rangle + |3, 1, 1\rangle$, the A-mode

set is the list of the a-modes in each term i.e $\{0, 1, 2, 3\}$ correspondingly the b-mode c-mode sets are $\{0, 0, 1, 1\}$ and $\{0, 1, 0, 1\}$.

Step 1: For a given $SRV(A,B,C)$ (A-B) terms have the same b-mode number and (A-C) terms have the same c-mode number.

As a reminder, the dimensionality of particles a,b,c is given by A,B,C respectively. This means that for a given $SRV(A,B,C)$ state particles a,b,c have A,B, and C different mode numbers respectively. Consequently, there are B terms with B different mode numbers (the mode set of these terms we will refer to as the independent set I_B). Accordingly, the b-mode set can be written as combination of an independent set I_B with $|I_B| = B$ and A-B terms that have a b-mode number that has appeared in those B terms, referred to as the non-independent set NI_B . Using the example state $SRV(4,2,2)$, I_B could be $\{0, 1\}$, while NI_B could be $\{0, 1\}$.

There are two possible ways to generate multiple terms with the same b-mode number. The first way is using graph II, which contains edge $E_{t,b}$. The second way is to let the term generated by graph I have the same b mode as a matching in graph III. Every term generated using a matching in graph III must have a different b-mode number or we will get two terms with the same b and c-mode numbers. The second method can generate one term that accounts for one mode in I_B and one term that accounts for a mode in NI_B where $|NI_B| = (A - B)$. This allocation does not have to be the case, but if the b-mode for the term generated using graph I is not the same as in graph III then all the modes in NI_B must be generated using graph II. All the terms generated using graph II have the same b-mode which which means there will be $|NI_B| = (A - B)$ terms with the same b-mode. Therefore, at least $(A - B - 1)$ terms in NI_B must have the same b-mode and are generated by perfect matchings in graph II. Since NI_B contains mode numbers present in I_B , the b-mode of one of these $(A - B - 1)$ terms must be identical to one mode number in I_B . Consequently, there are $(A - B)$ terms with the same b-mode number. The proof of this statement for c-modes is exactly the same as for b-modes with graph II and III switched.

Step 2: $A - B \leq C$

Say $(A - B) > C$ then there would be more than (A-B) terms with different c-mode numbers and (A-B) terms with the same b-mode number. Accordingly, there must be two terms with the same b and c mode number by the pigeonhole principle, which contradicts the repeat mode lemma.

Step 3: $C \leq A - B + 3$

At minimum $B-1$ terms are not generated by graph II since there are B different mode numbers and graph II can only generate terms with one b -mode number. Correspondingly, there are at minimum $C-1$ terms not generated by graph III since graph III can only generate terms with one c -mode number. There is only one term that is not generated by graph II and III corresponding to the one matching in graph I. Finally the total number of terms, A , must be greater than the total number of terms not generated by graph II or III using the principle of inclusion and exclusion this can be written as $(C - 1) + (B - 1) - 1 \leq A$. We can simply rearrange this inequality to arrive at the desired result.

References

- [1] I. Bogdanov. Graphs with only disjoint perfect matchings, 2017.
- [2] Agata M. Brańczyk. Hong-Ou-Mandel Interference, 2017.
- [3] Josh Cadney, Marcus Huber, Noah Linden, and Andreas Winter. Inequalities for the ranks of multipartite quantum states. *Linear Algebra and its Applications*, 452:153–171, jul 2014.
- [4] M.A.Horne D.M. Greenberger and A. Zeilinger. *Bell's Theorem, Quantum Theory and Conceptions of the Universe*. Springer, 1989.
- [5] Manuel Erhard, Mehul Malik, Mario Krenn, and Anton Zeilinger. Experimental greenberger–horne–zeilinger entanglement beyond qubits. *Nature Photonics*, 12(12):759–764, oct 2018.
- [6] Lan-Tian Feng, Ming Zhang, Di Liu, Yu-Jie Cheng, Guo-Ping Guo, Dao-Xin Dai, Guang-Can Guo, Mario Krenn, and Xi-Feng Ren. Observation of nonlocal quantum interference between the origins of a four-photon state in a silicon chip, 2021.
- [7] Xuemei Gu, Lijun Chen, and Mario Krenn. Quantum experiments and hypergraphs: Multiphoton sources for quantum interference, quantum computation, and quantum entanglement. *Physical Review A*, 101(3), mar 2020.
- [8] Xuemei Gu, Lijun Chen, Anton Zeilinger, and Mario Krenn. Quantum experiments and graphs. III. high-dimensional and multiparticle entanglement. *Physical Review A*, 99(3), mar 2019.

- [9] Armin Hochrainer, Mayukh Lahiri, Manuel Erhard, Mario Krenn, and Anton Zeilinger. Quantum Indistinguishability by Path Identity: The awakening of a sleeping beauty, 2021.
- [10] Marcus Huber and Julio I. de Vicente. structure of multidimensional entanglement in multipartite systems. 110(3), jan 2013.
- [11] Jakob S Kottmann, Mario Krenn, Thi Ha Kyaw, Sumner Alperin-Lea, and Alá n Aspuru-Guzik. Quantum computer-aided design of quantum optics hardware. *Quantum Science and Technology*, 6(3):035010, jul 2021.
- [12] Mario Krenn, Xuemei Gu, and Anton Zeilinger. Quantum Experiments and Graphs: Multiparty States as Coherent Superpositions of Perfect Matchings. *Physical Review Letters*, 119(24), dec 2017.
- [13] Mario Krenn, Jakob S. Kottmann, Nora Tischler, and Alá n Aspuru-Guzik. Conceptual understanding through efficient automated design of quantum optical experiments. *Physical Review X*, 11(3), aug 2021.
- [14] Mario Krenn, Mehul Malik, Robert Fickler, Radek Lapkiewicz, and Anton Zeilinger. Automated Search for new Quantum Experiments. *Physical Review Letters*, 116(9), mar 2016.
- [15] Noah Linden, Milá n Mosonyi, and Andreas Winter. The structure of rényi entropic inequalities. *Proceedings of the Royal Society A: Mathematical, Physical and Engineering Sciences*, 469(2158):20120737, oct 2013.
- [16] L.Mandel L.J.Wang, X.Y.Zou. Induced coherence without induced emission. *Physical Review A*, 44(7), 1991.
- [17] A. P. Lund, A. Laing, S. Rahimi-Keshari, T. Rudolph, J.L. O’Brien, and T.C. Ralph. boson sampling from a gaussian state. 113(10), sep 2014.
- [18] Mehul Malik, Manuel Erhard, Marcus Huber, Mario Krenn, Robert Fickler, and Anton Zeilinger. Multi-photon entanglement in high dimensions. *Nature Photonics*, 10(4):248–252, feb 2016.
- [19] Xuemei Gu Mario Krenn and Daniel Soltesz. Questions on the structure of perfect matchings inspired by quantum physics. 2019.

- [20] Jarrod R. McClean, Sergio Boixo, Vadim N. Smelyanskiy, Ryan Babush, and Hartmut Neven. Barren plateaus in quantum neural network training landscapes. *Nature Communications*, 9(1), nov 2018.
- [21] Alexey A. Melnikov, Hendrik Poulsen Nautrup, Mario Krenn, Vedran Dunjko, Markus Tiersch, Anton Zeilinger, and Hans J. Briegel. Active learning machine learns to create new quantum experiments. *Proceedings of the National Academy of Sciences*, 115(6):1221–1226, jan 2018.
- [22] Aaronson S. Scattershot BosonSampling: A new approach to scalable Boson-sampling experiments. <https://scottaaronson.blog/?p=1579>, 2013.
- [23] Sergei Slussarenko and Geoff J. Pryde. Photonic quantum information processing: A concise review. *Applied Physics Reviews*, 6(4):041303, dec 2019.
- [24] Leslie G Valiant. The complexity of enumeration and reliability problems. *SIAM Journal on Computing*, 1979.
- [25] L.Mandel X.Y.Zou, L.J. Wang. Induced Coherence and Indistinguishability in Optical Interference. *Physical Review Letters*, 67(3), 1991.